Available online at www.sciencedirect.com
ScienceDirect
International Journal of Mass Spectrometry 262 (2007) 33–44
International Journal of Mass Spectrometry
www.elsevier.com/locate/ijms

# Octupolar excitation of ion motion in a Penning trap—A study performed at LEBIT

R. Ringle [a,b,*], G. Bollen [a,b], P. Schury [a,b], S. Schwarz [a], T. Sun [a,b]

[a] *National Superconducting Cyclotron Laboratory, East Lansing, MI, USA*
[b] *Department of Physics and Astronomy, Michigan State University, East Lansing, MI, USA*

Received 12 September 2006; received in revised form 11 October 2006; accepted 12 October 2006
Available online 16 November 2006

**Abstract**

The excitation of the motion of ions in a Penning trap at twice their cyclotron frequency, $2\nu_c$, by means of an azimuthal octupolar rf field has been studied. Presented is the first experimental verification of such an rf octupolar excitation. Compared to ion excitation at $\nu_c$ by means of quadrupolar fields an increased resolving power is observed in the cyclotron resonance curves, which may have important implications for Penning trap mass measurements. Numerical simulations have been used to characterize important properties of this type of excitation in detail and to predict the behavior of the ion motion under realistic conditions. Good agreement with the experimental observations is observed. Furthermore, the quadrupolar excitation of the ion motion at $\nu_c$ has been revisited and its dependence on the phase of the ion motion and the rf field been studied.


*PACS:* 21.10.Dr; 34.50.Bw; 41.85.Ja; 29.25.Rm

*Keywords:* Penning trap; Ion motion; Octupolar excitation; Quadrupolar excitation; Resolving power

## 1. Introduction

Penning trap mass spectrometry has proven to be one of the most precise and accurate techniques for the determination of atomic masses of both stable and unstable nuclides. Mass accuracies of $10^{-10}$ and better have been achieved for stable isotopes [1–4], providing important data for metrology and QED tests. Mass measurements of unstable isotopes are of interest for nuclear structure studies, for providing key data for fundamental interaction tests, and for a better understanding of the nuclear synthesis of elements in our universe. Despite low production rates and short half-lives mass measurements of short-lived nuclides today reach accuracies of better than $10^{-8}$ [5,6]. One of the reasons that Penning traps have been so successful is that they are theoretically well understood [7–9].

Mass measurements in Penning traps are performed via the determination of the cyclotron frequency $\nu_c = (1/2\pi)(q/m)B$ of an ion with mass $m$ and charge $q$ stored in a strong magnetic field. The achievable precision $\delta\nu \propto (\nu \cdot T_{obs} \cdot \sqrt{N})^{-1}$ depends on the frequency $\nu$ to be observed, the observation time $T_{obs}$, and a statistical factor $\sqrt{N}$, where $N$ is the number of ions detected. In the case of rare isotopes half-lives can be as short as a few milliseconds and beam rates can be well below one ion per second. Since the half-life determines the observation time, gains in precision can only be achieved by maximizing $\nu \cdot \sqrt{N}$. Compared to improving statistics by increasing the number of measurements, if the beam rate is limited, the largest gain factor is obtained by increasing the frequency $\nu$ to be observed.

At present, all Penning trap mass spectrometers designed for the study of short-lived nuclides [10–15] employ a technique in which an azimuthal quadrupolar radiofrequency (rf) field is used to excite the radial motion of the ions in the trap [10,16]. At a frequency $\nu_{rf} = \nu_c = \nu_+ + \nu_-$ this field couples the (reduced) cyclotron motion and the magnetron motion, which have eigenfrequencies $\nu_+$ and $\nu_+$. In resonance, a change in energy can be obtained which is detected with a time-of-flight (TOF) resonance detection technique [17].

Several options exist for increasing the frequency $\nu$ to be observed. Going towards a higher magnetic field strength is a straightforward approach, realized in the case of LEBIT at the NSCL [11]. More complicated, but with substantial potential, is the employment of highly-charged ions as planned for the

* Corresponding author. Tel.: +1 5173336474.
*E-mail address:* ringle@nscl.msu.edu (R. Ringle).

1387-3806/$ – see front matter © 2006 Elsevier B.V. All rights reserved.
doi:10.1016/j.ijms.2006.10.009

TITAN [18] facility at TRIUMF. Another promising idea is to observe higher harmonics in the ion motion in the Penning trap, for example at twice the cyclotron frequency, $2\nu_c$.

General considerations lead one to conclude that an octupolar rf field with a frequency $\nu_{rf} = 2\nu_c$ will drive the ion motion in a resonant manner. One could also expect that the widths of the cyclotron resonances for both quadrupolar and octupolar excitation are in first order fourier-limited and should therefore be the same for a given observation time. In this case the octupolar excitation would yield a factor of two increase in resolving power over the quadrupolar excitation.

The Low Energy Beam and Ion Trap (LEBIT) facility at the NSCL at MSU is the first to perform Penning trap mass measurements on isotopes produced by in-flight separation of relativistic projectile fragments. In order to take full advantage of this fast production technique, LEBIT has been optimized towards sensitivity and reaching high precision and accuracy for very short-lived nuclides. LEBIT already uses a 9.4 T field, to be compared to 6–7 T used in most of the other systems. LEBIT has been designed to allow for the investigation of octupolar excitation. Early simulations [19] performed at MSU have indicated that octupolar excitation at $2\nu_c$ should indeed be possible and lead to an increase in resolving power.

In this work the first experimental verification of ion motion excitation with an octupolar rf field is presented together with a systematic study of the main features of this new excitation mode. So far no analytical solution has been found for the equations of motion. Therefore, very detailed numerical simulations have been performed to characterize this excitation mode. The simulation results are found to be in excellent agreement with the experimental observations. The most remarkable observation made both in experiment and simulations is a drastic increase in resolving power well beyond the expectation of the factor of two stated above. Similar observations have been made in an independent study [20] at SHIPTRAP at GSI, also presented in this volume. Hence, once fully established, octupolar excitation may provide a significant advance in Penning trap mass spectrometry, in particular for the study of short-lived isotopes.

In the simulation studies of octupolar excitation a strong phase dependence of the ion response was found. This motivated us to revisit the quadrupolar excitation. Both theoretically and experimentally we found that in the case of well-defined phase relations between the rf field and the initial ion motion the resonance shape can become asymmetric. This could provide a possible source of systematic errors in the mass determination if not considered appropriately, but also a tool for spectrometer diagnostics and tuning.

## 2. The LEBIT facility

The primary experimental goal of the LEBIT project is to perform high-precision mass measurements of rare isotopes produced by projectile fragmentation. For this purpose, relativistic rare isotope beams are converted into low-energy beams with excellent quality by using gas stopping and advanced ion guiding, cooling, and bunching techniques [21]. Mass measurements

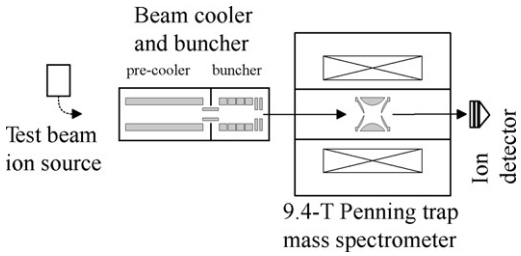


Fig. 1. Partial schematic of the LEBIT facility at the NSCL/MSU. Only components relating to the present work are shown.

are performed with the LEBIT Penning trap system. In the following a brief summary of the components of the LEBIT facility which are relevant to the present work will be presented.

Fig. 1 shows the components of the LEBIT facility used in the present study. LEBIT is equipped with a plasma ion source station. The plasma ion source provides beams of noble gasses and alkali metals. Most of the measurements presented in this work were performed using $^{23}Na^+$ and $^{39,41}K^+$. Those ions are transported to the LEBIT beam cooler and buncher [21,22]. The beam cooler and buncher consists of a pair of RFQ ion guide structures which converts the continuous beam delivered from the ion source into a cooled ion pulses which are then delivered to the Penning trap system [11], which features a 9.4 T persistent superconducting magnet. Located within the room-temperature bore is a high-precision hyperbolic electrode system, see Fig. 2, with a characteristic inner radius of $r_o = 13$ mm and a distance from trap center to the endcap electrodes of $z_o = 11.18$ mm. Holes in the endcaps allow the ions to be injected and ejected by switching the applied potentials to the appropriate endcap electrode. The ring electrode is eight-fold segmented allowing for the application of multipolar rf fields. Dipolar rf fields can be used for mass-selective ion removal. Quadrupolar rf fields applied at the proper frequency can be employed to excite the ion's motion at the ion's cyclotron frequency, $\nu_c$ [7]. Octupolar rf fields can also be applied, the study of which comprises a majority of this work.

Before the ion pulse from the buncher is captured in the Penning trap an initial magnetron motion is introduced, which

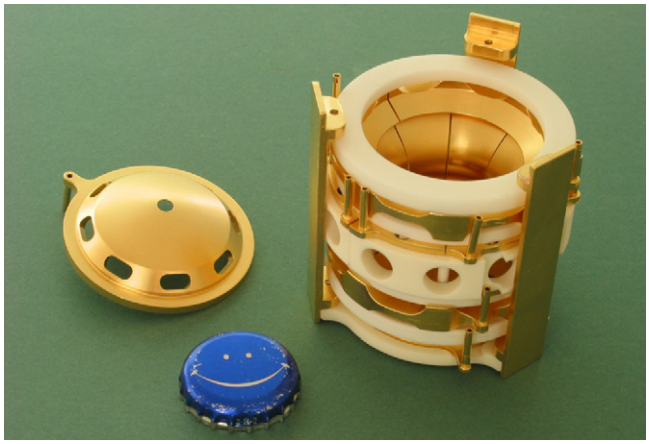

Fig. 2. The LEBIT high-precision Penning trap with the endcap electrode removed. Note the eight-fold segmentation of the hyperbolic ring electrode.

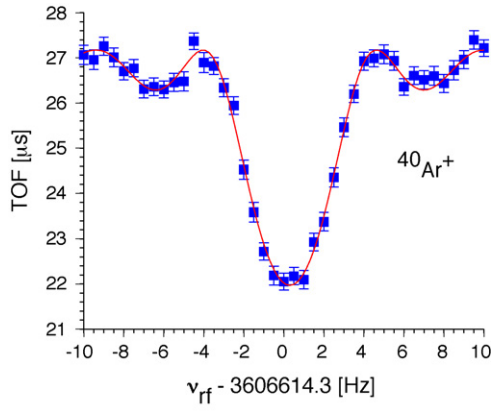


Fig. 3. Quadrupolar resonance curve of $^{40}Ar^+$ ions with a fit of the theoretical line shape. An excitation time of $T_{rf} = 200$ ms was used in this measurement. A full width $\Delta\nu_{FWHM} \approx 4.6$ Hz is observed.

is required previous to the application of a quadrupolar rf field. With LEBIT this is accomplished by employing an $\mathbf{E} \times \mathbf{B}$ drift technique using a so-called Lorentz steerer. This steerer is a quartered cylindrical tube at the end of the retardation optics preceding the Penning trap that can be used to create an electric dipole field perpendicular to the magnetic field.

After being captured the ions are exposed to an azimuthal quadrupolar rf field applied at a frequency $\nu_{rf}$ close to $\nu_c$. In the case where $\nu_{rf} = \nu_c$, choosing the appropriate rf amplitude and excitation time converts an initial magnetron motion into cyclotron motion, resulting in a gain of radial energy. The energy gain is then detected via a time-of-flight resonance detection technique [16,17,23] in which the ions are ejected from the trap and their time-of-flight to an ion detector, located outside of the magnetic field, is measured. While passing through the inhomogenous section of the magnetic field the radial energy gained during the excitation is converted into axial energy, reducing the time-of-flight to the detector. Repeating this process of trapping, excitation, ejection and time-of-flight measurement for different frequencies results in a resonance curve centered at $\nu_{rf} = \nu_c$. As an example, Fig. 3 shows a sample quadrupolar resonance of $^{40}Ar^+$ for an excitation time of $T_{rf} = 200$ ms. A full width, $\Delta\nu_{FWHM}$, of $\approx 0.9/T_{rf} = 4.5$ Hz is expected [16].

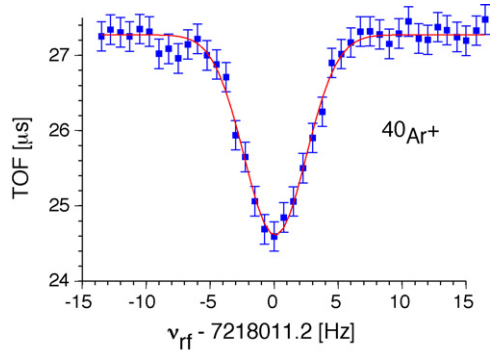


Fig. 4. Octupolar resonance curve of $^{40}Ar^+$ with a Gaussian fit. An excitation time of 200 ms was used in this measurement. A full width $\Delta\nu_{FWHM} \approx 4.8$ Hz is observed.

Soon after LEBIT had become fully operational the first octupolar excitation tests were performed. Fig. 4 shows one of the early resonances, obtained with an excitation of $^{40}Ar^+$ also using an excitation time of $T_{rf} = 200$ ms. A full width of $\Delta\nu_{FWHM} \approx 4.8$ Hz is observed, yielding a factor of two increase in resolving power over an equivalent quadrupolar excitation. However, as is discussed more fully in Section 4, simulations and additional measurements show that even greater increases in resolving power should be possible.

## 3. Aspects of the quadrupolar excitation

In order to provide some background for the discussion of both quadrupolar and octupolar excitations we will briefly review the major steps leading to the equations of motion for a quadrupolar excitation, as derived in [16].

### 3.1. Equations of motion

Begin by introducing the vectors $\vec{V}^+$ and $\vec{V}^-$ [9] such that

$$\vec{V}^{\pm} = \dot{\vec{\rho}} - \omega_{\mp} \cdot \vec{\rho} \times \hat{e}_z, \tag{1}$$

where $\vec{\rho}$ is the ion's position vector. Additionally,

$$\begin{aligned} x &= -\frac{V_y^+ - V_y^-}{\omega_+ - \omega_-} \\ y &= \frac{V_x^+ - V_x^-}{\omega_+ - \omega_-} \end{aligned}, \tag{2}$$

where $x$ and $y$ are the ion's position in Cartesian coordinates. Eq. (1) successfully decouples the equations of motion of an ion confined in a Penning trap. In the presence of an azimuthal, quadrupolar rf field these equations become

$$\begin{aligned} \dot{V}_x^{\pm} &= -\omega_{\pm} \cdot V_y^{\pm} + k \cdot (V_x^+ - V_x^-) \\ \dot{V}_y^{\pm} &= \omega_{\pm} \cdot V_x^{\pm} - k \cdot (V_y^+ - V_y^-) \\ k &= k_o \cdot \cos(\omega_{rf} t + \phi_{rf}), \quad \text{with } k_o = \frac{U_{rf}}{2a^2} \frac{q}{m} \frac{1}{\omega_+ - \omega_-} \end{aligned}. \tag{3}$$

Here $q$ is the ionic charge, $m$ the ionic mass, and $\phi_{rf}$ is the phase of the applied rf. The amplitude $U_{rf}$ corresponds to the maximum potential of the quadrupolar rf field on a circle of radius $a$. To first order $a$ is the inner radius of the trap, $r_o$. By applying the rotating wave approximation the equations of motion can be solved [16] and the solution is given by

$$\begin{aligned} \rho_{\pm}(t) = [\rho_{\pm,o} \cos(\omega_B t) \mp \frac{1}{2} \frac{\rho_{\pm,o}[i(\omega_{rf} - \omega_c)] + \rho_{\mp,o} k_o^{\pm}}{\omega_B} \\ \times \sin(\omega_B t)]\, e^{(i/2)(\omega_{rf} - \omega_c)t}, \end{aligned} \tag{4}$$

where $\rho_{\pm}(t)$ are the magnitudes of the cyclotron and magnetron radii as a function of time and $\rho_{\pm,o}$ are the initial cyclotron and magnetron radii. Additionally,

$$\omega_B = \frac{1}{2}\sqrt{(\omega_{rf} - \omega_c)^2 + k_o^2} \tag{5}$$

and $k_o^{\pm} = k_o\, e^{\pm i\Delta\phi}$. The phase relation, $\Delta\phi$, is given by

$$\Delta\phi = \phi_{rf} - (\phi_+ + \phi_-), \tag{6}$$

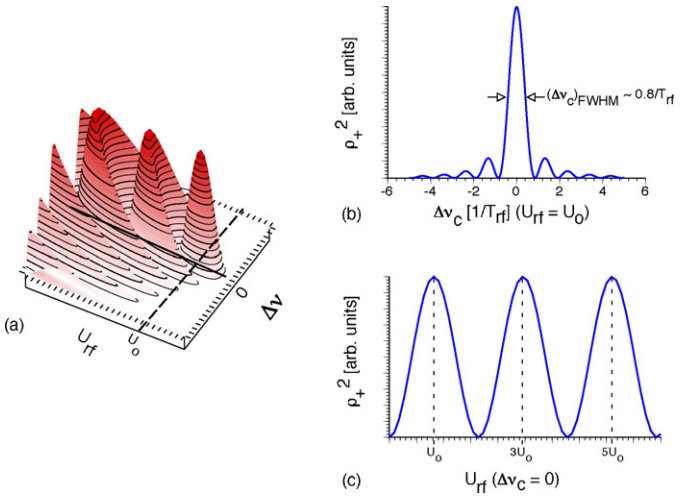


Fig. 5. (a) Surface plot of $\rho_+^2$ as a function of $U_{rf}$ and $\nu_{rf}$ for a given excitation time $T_{rf}$. (b) Cut from plot (a) at $U_{rf} = U_o$. Full conversion from magnetron to cyclotron motion is achieved at $\Delta\nu_c = \nu_{rf} - \nu_c = 0$. (c) Slice from plot (a) at $\Delta\nu = 0$ illustrating the beating of $\rho_+^2$ as a function of $U_{rf}$.

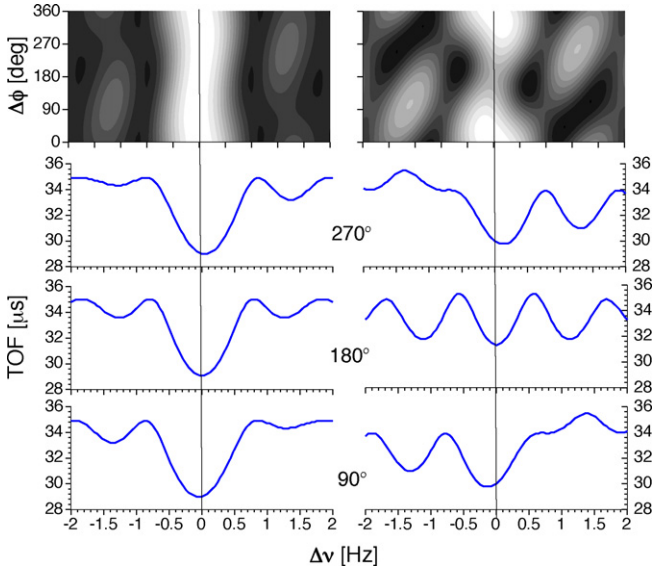


Fig. 6. Simulations of quadrupolar resonances for single $^{39}K^+$ ions with $T_{rf} = 1$ s. The two plots in the top row are contour plots of the resonances as a function of $\Delta\phi$ and $\Delta\nu$. Below are cuts at given values of $\Delta\phi$. Both simulations were performed with $\rho_{-,o} = 1$ mm and $\phi_{+,o} = \phi_{-,o} = 0°$. An initial cyclotron radius of $\rho_{+,o} = 0.1$ mm was used on the left and $\rho_{+,o} = 0.4$ mm was used on the right.

where $\phi_\pm$ are the cyclotron and magnetron phases. As stated above, radial energy gained during the excitation process is detected via a reduced time-of-flight of ions ejected from the trap to the detector. Under normal conditions $\omega_+ \gg \omega_-$, so we can write the radial energy as $E_r(t) \approx (1/2)m\omega_+^2 \rho_+^2(t)$.

Fig. 5(a) shows a calculated 3D plot of $\rho_+^2$, which is proportional to the gained energy, as a function of $U_{rf}$ and frequency detuning for a given $T_{rf}$ for a single ion initially executing pure magnetron motion, $\rho_{+,o} = 0$. Fig. 5(b) shows a cut at $U_{rf} = U_o$, which is the excitation amplitude at which a full conversion of magnetron to cyclotron motion has occurred for $\nu_{rf} = \nu_c$. Such a response is reflected in the experimental resonance curve shown in Fig. 3. Fig. 5(c) is a cut along $\Delta\nu = \nu_{rf} - \nu_c = 0$ illustrating the change of $\rho_+^2$ as a function of $U_{rf}$ for a constant excitation time.

When performing a quadrupolar excitation for a mass measurement one picks the appropriate combination of amplitude and excitation time, $U_{rf}$ and $T_{rf}$, such that the initial magnetron motion is fully converted into cyclotron motion, maximizing the radial energy gain of the trapped ions. The resulting line shape at this point has a full width, $\Delta\nu_{FWHM} \sim 0.8/T_{rf}$. Calculating the energy gain from the excitation and accounting for the ejection optics and magnetic field it is possible to calculate the theoretical line shape [16] to be observed in the time-of-flight measurement. This shape has been used to fit the experimental data shown in Fig. 3. Due to a nonlinear conversion between radial energy and time-of-flight, the full width of the time-of-flight curve is $0.9/T_{rf}$ for LEBIT.

### 3.2. Phase dependence of the quadrupolar excitation

The solution to the equations of motion as derived in [16] contains a phase dependence, the consequence of which has not been previously investigated. The phase-dependent term appears in Eq. (4) through the $k_o^\pm$ term. We algebraically expand

$$\rho_+(t)\rho_+(t)^* = \frac{4\rho_{+,o}^2\omega_B^2\cos^2(\omega_B t)}{4\omega_B^2} + \frac{k_o^2\rho_{-,o}^2 + \rho_{+,o}^2(\omega_{rf} - \omega_c)^2}{4\omega_B^2} \times \sin^2(\omega_B t) - \frac{k_o\rho_{-,o}\rho_{+,o}(\omega_{rf} - \omega_c)\sin(\Delta\phi)}{4\omega_B^2} \times \sin^2(\omega_B t) - \frac{2k_o\rho_{-,o}\rho_{+,o}\omega_B\cos(\Delta\phi)}{4\omega_B^2} \times \sin(2\omega_B t). \quad (7)$$

The phase dependence of the radial energy change is located in the third and fourth terms of Eq. (7). Both terms scale with the product of $\rho_{+,o}$ and $\rho_{-,o}$, which means if the ions begin in a state of pure cyclotron or magnetron motion at the beginning of the excitation the effect will not be present.

Fig. 6 presents the results of simulations of quadrupolar resonances for single $^{39}K^+$ ions with $T_{rf} = 1$ s. Both simulations were performed with $\rho_{-,o} = 1$ mm and $\phi_{+,o} = \phi_{-,o} = 0°$. An initial cyclotron radius of $\rho_{+,o} = 0.1$ mm was used on the left and $\rho_{+,o} = 0.4$ mm was used on the right. In each case the value of $U_{rf}$ was adjusted such that in resonance and for $\phi_{rf} = 0°$ the radial energy was maximized. Looking closely at the contour plot on the left one can see a distortion of the central peak and a shift in the position of the side bands as $\Delta\phi$ changes. Resonance profiles for which $\Delta\phi = 90$ and 270° become asymmetric and the position of the minimum time-of-flight has shifted slightly. Increasing the value of $\rho_{+,o}$ to 0.4 mm only exacerbates the situation. The most obvious implication of these phase-dependent effects involve low-statistics measurements where $\Delta\phi$ is allowed to vary. If the measurement samples any particular phase range more frequently and the resonance is fit with a line

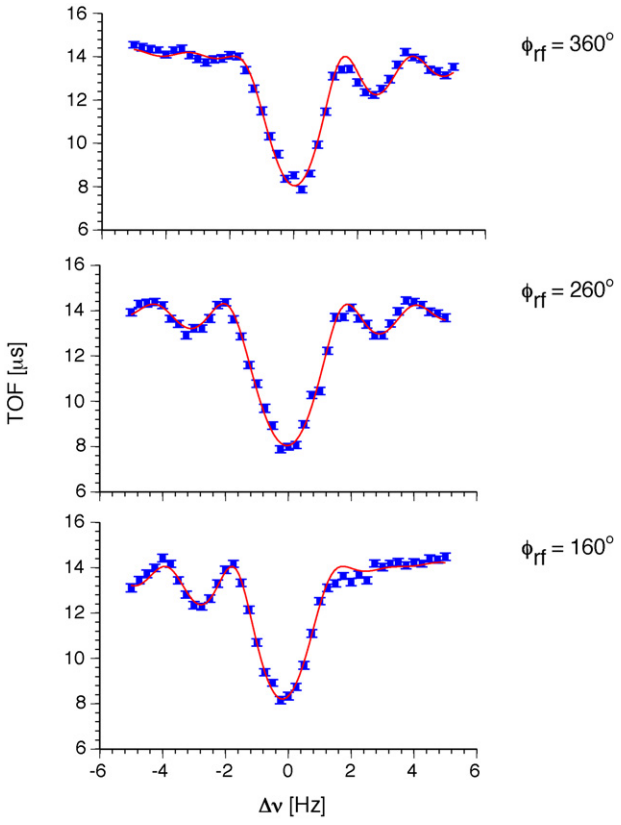


Fig. 7. Three $^{39}K^{+}$ quadrupolar resonances for $T_{rf} = 500$ ms measured for different values of $\phi_{rf}$. The solid line is the fit of the theoretical line shape.

shape with a symmetric center then the analysis will include an additional error.

In order to see the phase dependence in the radial energy change of the quadrupolar excitation, two conditions must be met. The first is that the rf voltage must have a defined phase relation to initial ion motion. $\Delta\phi$ must not be random which means, according to Eq. (6), that all individual phases must be well defined. If this is not the case then the final line shape will be an average over the line shapes of random $\Delta\phi$'s. The second condition is that the ion ensemble cannot begin in a pure state of cyclotron or magnetron motion.

For the test of this phase dependence $^{39}K^{+}$ ions were injected into the Penning trap, and an initial magnetron motion was introduced with the Lorentz steerer. The excitation rf was phase locked to the time of ion capture in the trap, which defines the initial phase of the ion motion. Several resonances with $T_{rf} = 500$ ms were taken with varied values of $\phi_{rf}$. Fig. 7 illustrates the effect of varying $\phi_{rf}$ on the resonance shape. Here we see experimentally how the sidebands change shape as the value of $\Delta\phi$ is changed. When $\Delta\phi$ is allowed to be a free parameter a good agreement is seen between the experimental data and the fit. All three fits yield consistent values for $\rho_{-,o} = 0.91(2)$ mm and $\rho_{+,o} = 0.11(1)$ mm. For each resonance $\phi_{rf}$ was incremented by 100°. Within 20% this phase dependence was reproduced in the fit parameter $\Delta\phi$.

As discussed earlier, only the third and fourth terms of Eq. (7) contain a $\Delta\phi$ term and contain the product of $\rho_{+,o}$ and $\rho_{-,o}$. While $\rho_{-,o}$ is introduced deliberately, a finite $\rho_{+,o}$ must be the result of an asymmetric injection of ions into the magnetic field of the Penning trap which leads to a pickup of cyclotron motion. If the amount of radial energy gained during the injection process can be reduced, then $\rho_{+,o}$ will be reduced, thus reducing the phase-dependent effect. This could be useful in fine-tuning the injection of ions into a Penning trap.

## 4. Octupolar excitation

Excitation of ion motion in a Penning trap by application of an octupolar rf field at frequencies near $2\nu_c$ have been studied experimentally and in simulation. Single-ion simulations are used to explore the resonant response of $\rho_+^2$ for a variety of initial conditions. Simulations utilizing realistic distributions of multiple ions are used to predict resonance profiles under realistic conditions. Two independent codes were developed and used in these studies: a fourth-order Runge–Kutta routine written in Fortran and compiled on a Windows machine, and a fourth-order Runge–Kutta routine with adaptive step size control written in C++ and compiled on an OSX machine.

Experimental results together with those from simulation are used to make estimates of the distribution for initial conditions. In many cases 2D simulation results have been presented to illustrate the scope of the simulations performed. In practice, though, the agreement between experimental and simulation data is more clearly observed by presenting projections of the data.

### 4.1. Equations of motion

Calculating the electric field produced by a time-varying octupolar field produced by a set of electrodes at a radius $a$ from the trap center yields the following field components:

$$\begin{aligned} E_x &= \frac{U_{rf}}{a^4}\sin(\omega_{rf}t+\phi_{rf})(y^3-3x^2y) \\ E_y &= -\frac{U_{rf}}{a^4}\sin(\omega_{rf}t+\phi_{rf})(x^3-3xy^2) \end{aligned} . \tag{8}$$

Writing out the full equations of motion of an ion in a Penning trap subjected to an octupolar rf field using the transformation given in Eq. (2) yields

$$\begin{aligned} \dot{V}_x^{\pm} &= -\omega_{\pm}V_y^{\pm} - k\frac{(V_x^+ - V_x^-)^2[(V_x^+ - V_x^-)^2 - 3(V_y^+ - V_y^-)^2]}{(\omega_+ - \omega_-)^3} \\ \dot{V}_y^{\pm} &= \omega_{\pm}V_x^{\pm} + k\frac{(V_y^+ - V_y^-)^2[(V_y^+ - V_y^-)^2 - 3(V_x^+ - V_x^-)^2]}{(\omega_+ - \omega_-)^3} \end{aligned} \tag{9}$$

where

$$k = \frac{U_{rf}}{a^4}\frac{q}{m}\sin(\omega_{rf}t+\phi_{rf}). \tag{10}$$

Unfortunately, the transformation does not decouple the equations of motion. The ansatz presented in [16], $\vec{V}^{\pm} = \vec{A}^{\pm}(t)\,e^{\pm i(\omega_{\pm}+\phi_{\pm})}$, where $A^{\pm}$ is an amplitude, does not simplify the problem. In the case of the quadrupolar excitation after the ansatz is inserted the high-frequency components can be neglected and the solution remains a physical description of

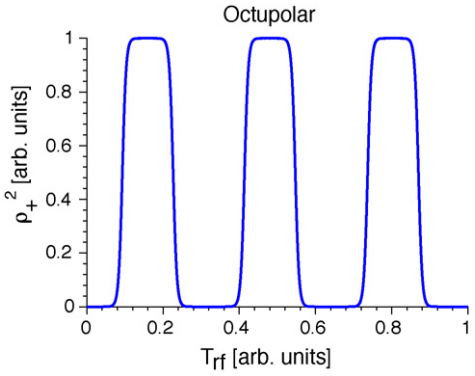


Fig. 8. $\rho_+^2$ of an ion confined in a Penning trap and subjected to an azimuthal octupolar rf field at frequency $2\nu_c$.

the system. Following the same procedure in the case of the octupolar excitation yields a non-physical description of the system. Unless a suitable coordinate transformation is found an analytical solution may not be possible. Numerical solutions to the equations of motion have to be used. By calculating the vectors $\vec{V}^{\pm}$ and using Eq. (1) it is possible to extract $\rho_+$ and $\rho_-$ as a function of time. Since $E_r \propto \rho_+^2$, the radial energy pickup due to the application of an octupolar rf field is directly accessible.

### 4.2. Single-ion octupolar simulations

Octupolar excitation of the motion of a single ion will be used to illustrate the similarities and differences between the octupolar and quadrupolar excitation schemes.

#### 4.2.1. Motional beating of single ions with $\nu_{rf} = 2\nu_c$

Fig. 8 plots $\rho_+^2$ of an ion as a function of time subjected to an azimuthal octupolar rf field. The ion is initially in a state of pure magnetron motion. A periodic beat pattern is observed. Compared to the quadrupolar case (Fig. 5c) the beating is no longer harmonic but begins to approach a square wave in shape.

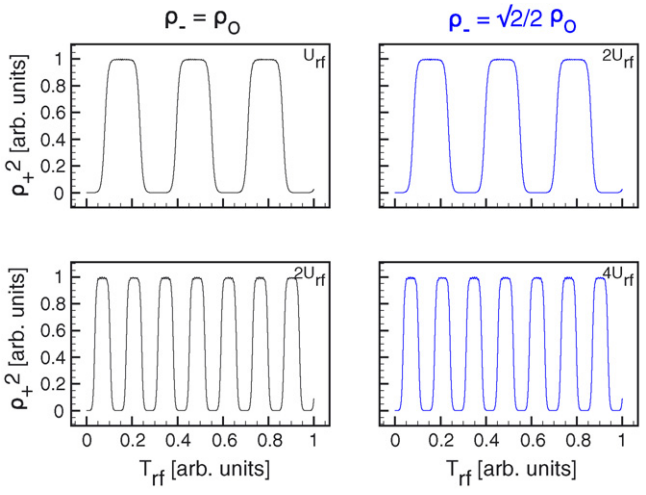


Fig. 9. The left hand plots show $\rho_+^2$ as a function of $T_{rf}$ for an ion with an initial $\rho_{-,o} = \rho_o$ and $\rho_{+,o} = 0$ with applied rf amplitudes of $U_{rf}$ and $2U_{rf}$, respectively. The right hand plots $\rho_+^2$ for an ion with an initial $\rho_{-,o} = (\sqrt{2}/2)\rho_o$ and applied rf amplitudes of $2U_{rf}$ and $4U_{rf}$, respectively.

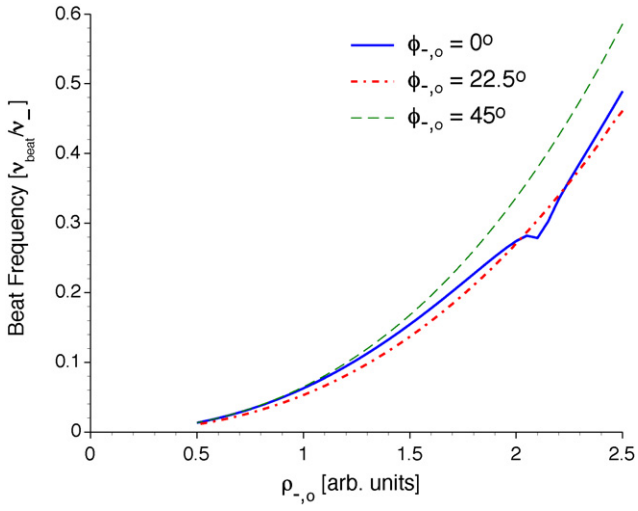


Fig. 10. Beat frequency between magnetron and cyclotron motions as a function of $\rho_{-,o}$ for constant $U_{rf}$ and for three initial magnetron phases, $\phi_{-,o} = 0$, 22.5 and 45°.

According to Eq. (5), the beat frequency of an ion induced by a quadrupolar rf field with $\nu_{rf} = \nu_c$ is proportional to $U_{rf}$, and independent of the initial ion motion. This is not the case with the octupolar excitation. Fig. 9 displays the $\rho_+^2$ of a single ion, subjected to an octupolar field with $\nu_{rf} = 2\nu_c$, for different initial magnetron radii, $\rho_{-,o}$, and applied rf amplitudes, $U_{rf}$. The plots on the left hand display the beat patterns for an ion with an initial arbitrary magnetron radius $\rho_o$. Doubling $U_{rf}$ results in an increase in the beat frequency. The plots on the right illustrate that doubling $U_{rf}$ and scaling the initial magnetron radius by $\sqrt{2}/2$ preserves the original beat frequency. In the case of octupolar excitation the beat frequency depends not only on the excitation amplitude, but also on the initial motion of the ion in the trap.

Fig. 10 plots the beat frequency as a function of the initial $\rho_{-,o}$ for three different initial magnetron phases, $\phi_{-,o}$. The figure reveals that the beat frequency depends not only on $\rho_{-,o}$, but also on $\phi_{-,o}$. The dip in the $\phi_{-,o} = 0°$ curve is not a numerical artifact, but has been produced by both codes for a range of numerical precisions used. By changing the phase one can change the position of this dip, but quickly moves to a larger value of $\rho_{-,o}$ as one moves away from $\phi_{-,o} = 0°$. With $\phi_{rf} = 0°$ the dip occurs at $\rho_-$ ~2.1 and $\nu_{beat}/\nu_-$ ~0.26. Fig. 9 might lead one to believe that $\nu_{beat} \propto \rho_{-,o}^2 \cdot U_{rf}$, yet taking Fig. 10 into account the relation would need to be amended to $\nu_{beat} \propto f(\phi_-) \cdot \rho_{-,o}^2 \cdot U_{rf}$. Holding $U_{rf}$ and $\phi_{-,o}$ constant and plotting the beat frequency as a function of $\phi_{-,o}$ yields Fig. 11. The beat frequency seems to sample the octupolar rf field's spatial orientation, and is at a minimum at the anti-nodes, and maximum at the nodes, of the field.

According to Eq. (5) the beat frequency in the case of $\nu_{rf} = \nu_c$ due to a quadrupolar excitaton is linear with respect to $U_{rf}$ and is phase independent. Again, this is different in the case of octupolar excitation. The beat frequency is not linear with respect to $U_{rf}$, and is dependent upon the $\phi_{-,o}$, as is illustrated in Fig. 12 which plots the beat frequency as a function of $U_{rf}$. As the beat frequency nears $\nu_-$ the beat

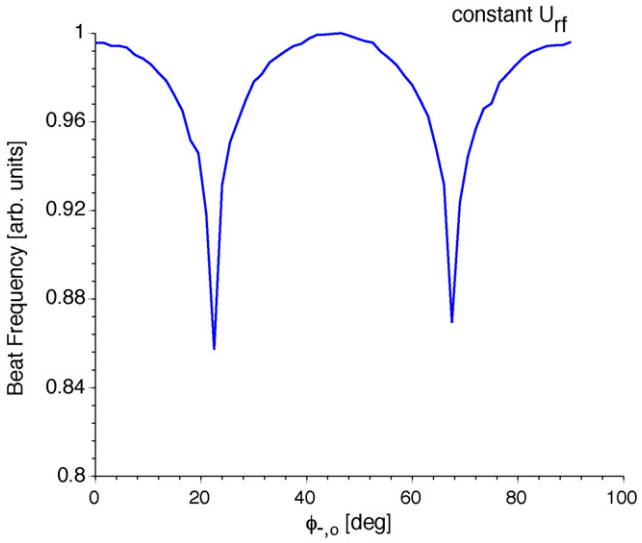


Fig. 11. Beat frequency as a function of $\phi_{-,o}$ for a constant $U_{rf}$.

pattern begins to lose its periodic nature. Zooming in to low frequencies and excitation amplitudes the $\phi_{-,o} = 0^\circ$ and $\phi_{-,o} = 45^\circ$ curves become indistinguishable, while the $\phi_{-,o} = 22.5^\circ$ curve deviates. Again, similar to Fig. 10, a dip is observed in the $\phi_{-,o} = 0^\circ$ case, again located at $\nu_{beat}/\nu_- \sim 0.26$.

We are now in a position to investigate a possible invariant of the motion. Fig. 13 shows the beat frequency when changing $\rho_{-,o}$, while at the same time keeping the product $U_{rf} \cdot \rho_{-,o}^2$ constant. It can be seen that the beat frequency is constant for a given initial phase, $\phi_{-,o}$. This was found to be not only true for ions in a state of pure magnetron motion, but for mixed initial motions, $\rho_o = \sqrt{\rho_{+,o}^2 + \rho_{-,o}^2}$, as well. Therefore, we arrive at a general relationship $\nu_{beat} \propto \alpha(\rho_{\pm,o}, \phi_{\pm,o}, \phi_{rf}) \cdot \rho_o^2 \cdot U_{rf}$, where $\alpha$ is a scaling factor which depends on all four of the initial $\rho$'s and $\phi$'s.

### 4.2.2. Invariant phase relation of the octupolar excitation

According to Eq. (6), $\Delta\phi = \phi_{rf} - (\phi_+ + \phi_-)$ is a constant of the motion for a quadrupolar excitation. We investigate if a similar phase relation holds for the octupolar excitation.

Fig. 14 shows scans of $\rho_+^2$ as a function of $\phi_{+,o}$ and time for a given $\phi_{-,o}$ with $\phi_{rf} = 0^\circ$ in all cases. By comparing the patterns

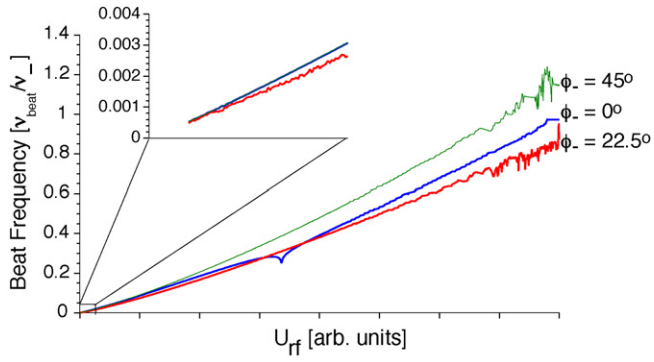


Fig. 12. Beat frequency as a function of $U_{rf}$ for three initial $\phi_{-,o}$'s. The insert zooms in to low beating frequencies and amplitudes.

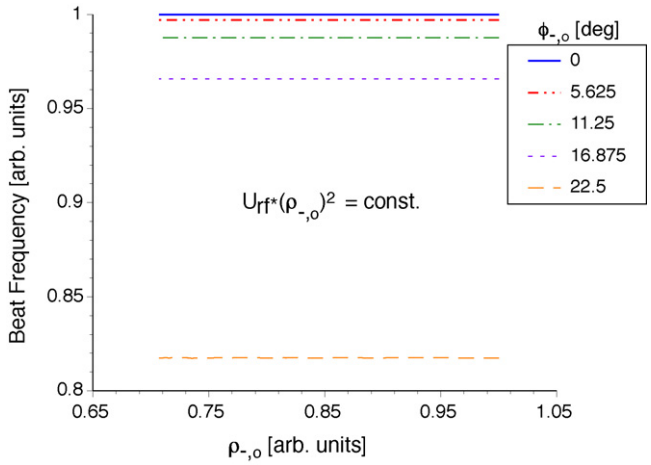


Fig. 13. Beat frequency due to an octupolar excitation as a function of $\rho_{-,o}$ holding $\rho_{-,o}^2 \cdot U_{rf}$ constant for several values of $\phi_{-,o}$.

it is easy to conclude that the time dependence of $\rho_+^2$ is the same if $\phi_{+,o} + \phi_{-,o} = \text{const}$. It was verified that this also holds true if $\phi_{rf}$ is changed.

Fig. 15 is similar to Fig. 14, except $\phi_{+,o}$ is held constant at $0^\circ$ and the individual plots are $\rho_+^2$ as a function of $\phi_{-,o}$ and time. Here we verified that for $\phi_{+,o} = 0^\circ$, $(1/2)\phi_{rf} - \phi_{-,o} = \text{constant}$ the same time dependence of $\rho_+^2$ is observed. Testing this condition for many values of $\phi_{+,o}$ yields the same results and leads us to conclude that the invariant phase in the case of octupolar excitation is $\Delta\phi = (1/2)\phi_{rf} - (\phi_+ + \phi_-)$. This

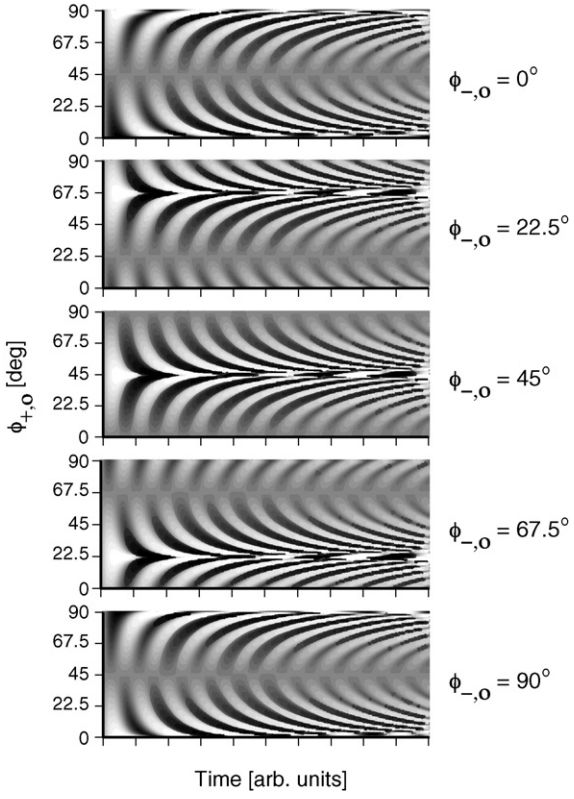


Fig. 14. 2D simulations of $\rho_+^2$ as a function of time and $\phi_{+,o}$ for a given $\phi_{-,o}$ with $\phi_{rf} = 0^\circ$. The grey scale is proportional to $\rho_+^2$.

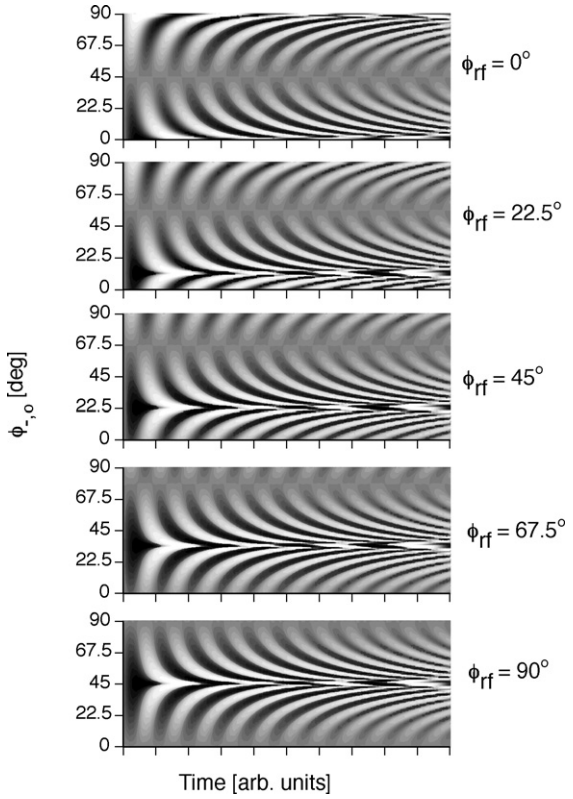


Fig. 15. 2D simulations of $\rho_+^2$ as a function of time and $\phi_{-,o}$ for a given $\phi_{rf}$ with $\phi_{+,o} = 0°$. The grey scale is proportional to $\rho_+^2$.

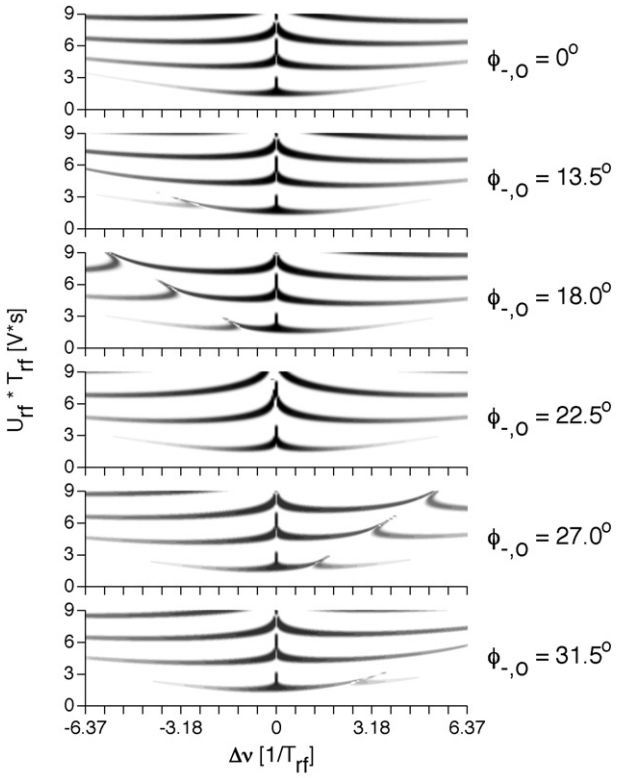


Fig. 16. Simulation of $\rho_+^2$ for a single ion with $\rho_{-,o} = 1$ mm and $\rho_{+,o} = 0$ mm as a function of frequency detuning, $\Delta\nu = \nu_{rf} - 2\nu_c$, and $U_{rf}$ for different values of $\phi_{-,o}$. The grey scale is proportional to $\rho_+^2$.

differs from the quadrupolar phase relation, Eq. (6), only in the factor of 1/2 multiplying the $\phi_{rf}$ term. This appears plausible as the octupolar field has twice the number of nodes and anti-nodes as the quadrupolar field. The factor of 1/2 reflects that the ions begin their motion at the same position with respect to the field orientation.

*4.2.3. Single-ion resonance curves*

To begin, we will examine octupolar resonances of single ions initially in a state where $\rho_o = \rho_{-,o}$. The general observation is a periodic change of $\rho_+^2$ as a function of $U_{rf}$. Along the line $\nu_{rf} = 2\nu_c$ a resonant effect is observed. Fig. 16 illustrates the dependence of $\rho_+^2$ on frequency detuning, $\Delta\nu = \nu_{rf} - 2\nu_c$, and $U_{rf}$ for various values of $\phi_{-,o}$. At $\phi_{-,o} = 13.5°$ a secondary resonant effect becomes visible which sweeps through the primary resonant structure as the value of $\phi_{-,o}$ is changed. This effect is on a line with an origin at $U_{rf} = 0$ and $\Delta\nu = 0$ which rotates clockwise for increasing values of $\phi_{-,o}$. At $\phi_{-,o} = 18.0°$ the structure can be seen across all three sections of the primary resonant structure. At $\phi_{-,o} = 22.5°$ the secondary structure lies on the $\Delta\nu = 0$ line.

Looking closely at the resonances reveals a narrowing of the resonance profiles at $\Delta\nu = 0$ for certain values of $U_{rf}$. Fig. 17 plots 2D cuts from the $\phi_{-,o} = 0°$ (left) and $\phi_{-,o} = 22.5°$ (right) cases shown in Fig. 16. Moving from the top plots to the bottom steps through the first conversion of magnetron to cyclotron motion. The $\phi_{-,o} = 0°$ case exhibits a larger width in the radial energy distribution at the lower values of $U_{rf} \cdot T_{rf}$ as in $\phi_{-,o} = 22.5°$ case. The central peak narrows for larger values of $U_{rf} \cdot T_{rf}$ and at $U_{rf} \cdot T_{rf} = 2.90$ V s the radial energy gained during the excitation begins to drop. The top three plots of the $\phi_{-,o} = 22.5°$ case show a suppression of radial energy at $\Delta\nu \approx 2\nu_c$. The bottom three plots no longer exhibit this behavior, but the central peak continues to narrow. In both

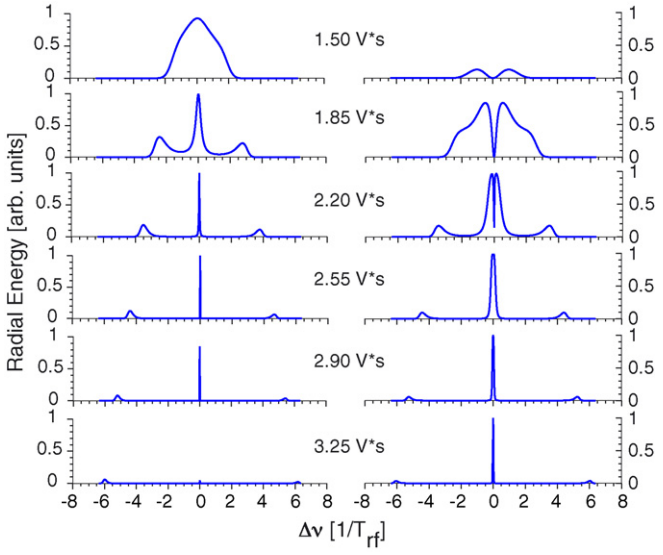


Fig. 17. 2D cuts from the $\phi_{-,o} - = 0°$ and $\phi_{o,-} - = 22.5°$ 3D profiles in Fig. 16 for six different values of $U_{rf} \cdot T_{rf}$.

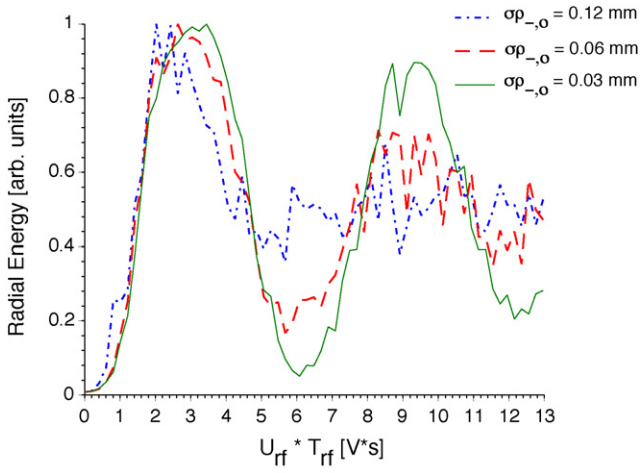


Fig. 18. Simulated radial energy gain for three different values of $\sigma_{\rho_{-,o}}$ as a function of $U_{rf}$ for $\nu_{rf} = 2\nu_c$ and $\bar{\rho}_- = 0.55$ mm.

cases $\Delta\nu_{FWHM}$ falls below $1/(100 \cdot T_{rf})$, which corresponds to a factor of ~200 increase in resolving power over the quadrupolar excitation for the same excitation time! It remains to be seen how well the ions can be prepared to reproduce these results under realistic conditions.

#### 4.2.4. Realistic multi-ion simulations

Simulations involving multiple ions representing a cloud are required to study the ion behavior in the case of an octupolar excitation under realistic conditions. First we will examine the radial energy gain as a function of $U_{rf}$, with $\nu_{rf} = 2\nu_c$. Gaussian distributions were used in generating values for the initial ion cloud. Fig. 18 shows the results of three simulations for three different values of $\sigma_{\rho_{-,o}}$ with $\bar{\rho}_{-,o} = 0.55$ mm. $\rho_{+,o} = 0.050(5)$ mm was used, being a conservative estimate from simulated radial energy gain during injection into the Penning trap. This value also agrees with those obtained from fits to quadrupolar resonances obtained under similar conditions. Widths of the $\phi$ distributions seem to have a small effect on the multi-ion response curves, and $\phi_- = 0(5)^\circ$ and $\phi_+ = 0(50)^\circ$ were used. For the largest value of $\sigma_{\rho_{-,o}}$ shown in Fig. 18 the curve seems to mimic the behavior of a damped oscillator, converging to some average asymptotical value of radial energy. This is the result of the beat frequency being dependent on $\rho_o$, as discussed in Section 4.2.1. The larger the spread in $\rho_o$, the larger the range of beat frequencies. The distribution of beat frequencies determines how quickly the average beat pattern is damped.

Fig. 19 plots the results from two octupolar simulations of $^{23}Na^+$ with $T_{rf} = 50$ ms. Both simulations were performed with identical phase and $\rho_+$ distributions as the simulations shown in Fig. 18. $\bar{\rho}_-$ was also held constant, but the widths of the distributions were changed. The simulation in the first column was performed with $\rho_{-,o} = 0.8000(325)$ mm and the the second with $\rho_{-,o} = 0.80(13)$ mm. Instead of $\rho_+^2$ the calculated time-of-flight was plotted for easier comparison to experimental results covered in the next section. The plots in the first row show the dependence of the time-of-flight as a function of $U_{rf}$ and $\Delta\nu$.

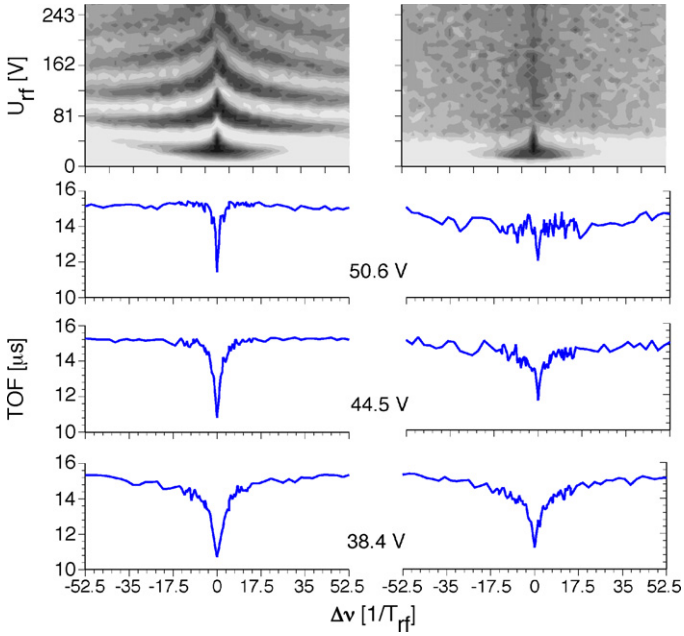


Fig. 19. (Left) multi-ion simulation of TOF as a function of $U_{rf}$ and $\Delta\nu$ with three cuts at different rf voltages. (Right) same as the left only the width of the $\rho_{-,o}$ distribution has been increased by a factor of 4.

The grey scale indicates smaller values of time-of-flight. The plots in the remaining rows are cuts at different voltages.

Note the resemblance of the top left plot to the single-ion case shown in Fig. 16. For the larger $\sigma_{\rho_{-,o}}$, shown on the right, only one conversion is seen in the grey-scale plot before settling down to an average value. This is also reflected in Fig. 18. The 2D profiles also reveal that there is a greater separation in time-of-flight between the baseline and the minimum for the profiles on the left. In both cases as one proceeds from smaller to larger values of $U_{rf}$ the resonance narrows. On the right-hand side the narrow peak begins to develop on top of a broader resonant structure, while on the left the time-of-flight baseline does not change. At $U_{rf} = 44.5$ V the resonance curve on the left has achieved a maximum change in time-of-flight and a minimal width of $\sim 0.14/T_{rf}$, corresponding to a gain of a factor of 13 in resolving power over the quadrupolar excitation.

### 4.3. Experimental procedure and results

Fig. 20 presents a schematic drawing of the electronic setup which was used to produce an azimuthal octupolar rf field in the LEBIT Penning trap. An arbitrary function generator (AFG) prodives a signal to a broadband rf amplifier with 65 dB gain. The signal from the amplifier is fed into a phase-splitting coil. The two output signals, $U_{rf,1}$ and $U_{rf,2}$, which are 180° out of phase, are then fed into the ring electrode segments. The amplitudes of the two phases agree to within ~15–20 %. From now on, their average will be quoted as the excitation amplitude, $U_{rf}$.

In the experiments $^{23}Na^+$ ions were used. Ion bunches from the cooler/buncher were injected off-axis, via the Lorentz steerer, mentioned above, and trapped in the LEBIT high-precision Penning trap.

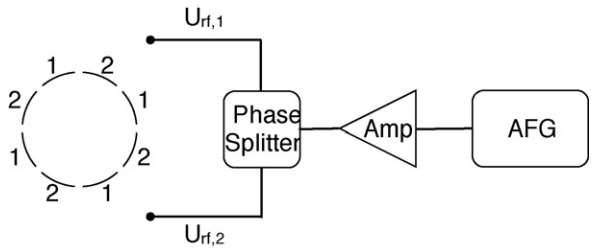


Fig. 20. Schematic drawing of experimental setup used to produce a azimuthal octupolar rf field in the LEBIT Penning trap.

*4.3.1. Experimental octupolar studies in resonance*

$^{23}Na^{+}$ ions were excited with an octupolar excitation with $\nu_{rf} = 2\nu_c$ for $T_{rf} = 50$ ms and their time-of-flight was measured as a function of $U_{rf}$. The result is shown in Fig. 21 together with a simulated curve. The simulated curve corresponds to the $\sigma_{\rho_{-,o}} = 0.13$ mm case from Fig. 18. In order to get a good agreement between experimental data and the simulation results it was necessary to divide rf voltage values measured at the output of the circuit by a factor of 0.7. Such a factor makes sense as it accounts for rf attenuation and partial shielding due to the geometry of the trap. Using experimental data like that shown in Fig. 21 and comparing to the corresponding simulation results allows the values of $\bar{\rho}_{-,o}$ and $\sigma_{\rho_{-,o}}$ to be determined. The minimum time-of-flight value achieved is a function, primarily, of $\bar{\rho}_{-,o}$, and the damping of the curve is determined by the ratio of $\sigma_{\rho_{-,o}}$ and $\bar{\rho}_{-,o}$.

In the case of quadrupolar excitation, the beat frequency of $\rho_+^2(t)$ is proportional to the product $U_{rf} \cdot T_{rf}$ (see Eq. (5)). We will experimentally explore if this holds true for the octupolar excitation, as well. Fig. 22 plots time-of-flight of ions as a function of $U_{rf}$ for five different excitation times. As expected, the minimum time-of-flight is reached at a lower value of $U_{rf}$ for longer excitation times. The value of $U_{rf}$ where the TOF curve reaches its minimum was determined visually, and will be labeled $U_o$. Fig. 23 displays the product $U_o \cdot T_{rf}$ for the fives cases shown in Fig. 22, along with simulated data using

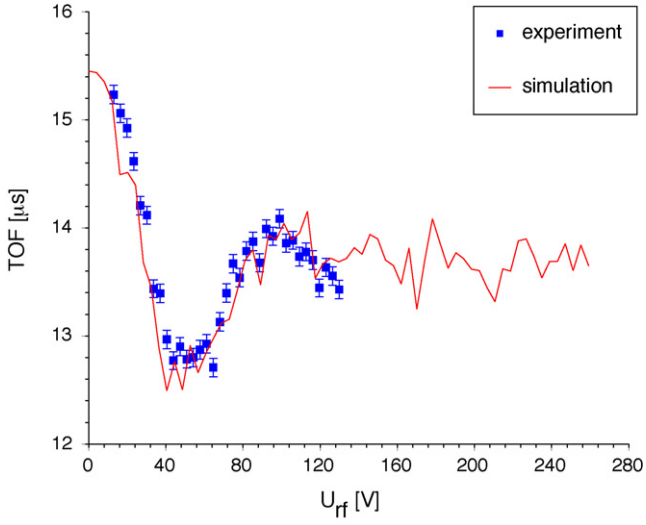


Fig. 21. Time-of-flight as a function of $U_{rf}$ for a octupolar excitation of $^{23}Na^{+}$ with $T_{rf} = 50$ ms at $\nu_{rf} = 2\nu_c$. The solid line shows a simulation.

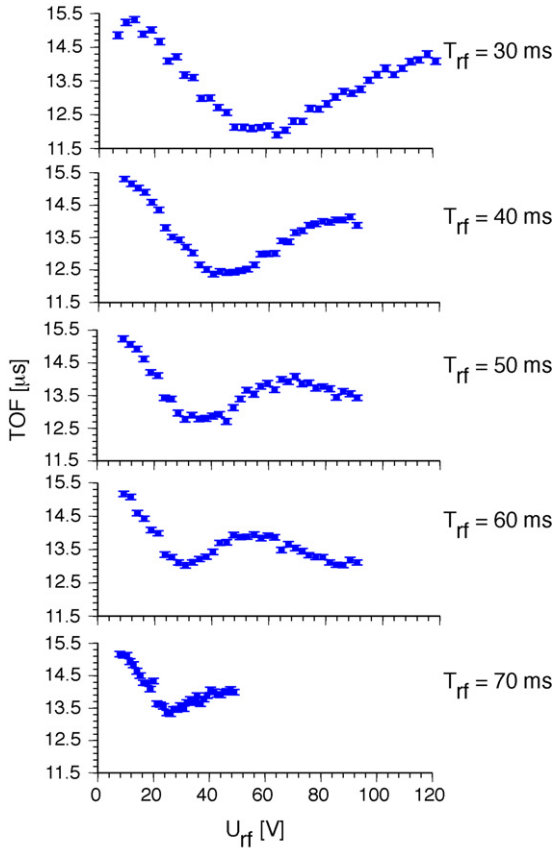


Fig. 22. Octupolar TOF curves of $^{23}Na^{+}$ as a function of $U_{rf}$ with $\nu_{rf} = 2\nu_c$ for several excitation times.

our best-fit parameters determined by the comparison shown in Fig. 21. The minima of the simulated TOF curves were also inspected visually. Within an estimated uncertainty of 5% for both simulation and experiment the data agree and are constant.

By adjusting the Lorentz steerer we can control $\bar{\rho}_{-,o}$. The displacement of the ions as a function of the applied voltage is linear. Fig. 24 shows six different octupolar scans of TOF as

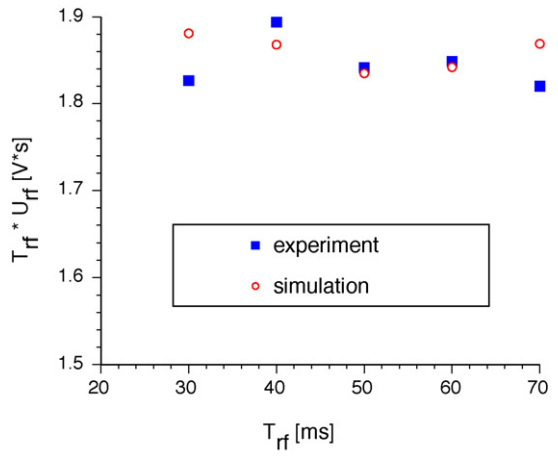


Fig. 23. Product of $U_o$ and $T_{rf}$, where $T_{rf}$ is the duration of the octupolar excitation and $U_o$ is the amplitude of applied octupolar rf field at which the TOF curve reaches its minimum. Experimental and simulation uncertainties (not shown for clarity) are estimated to be about 5%.

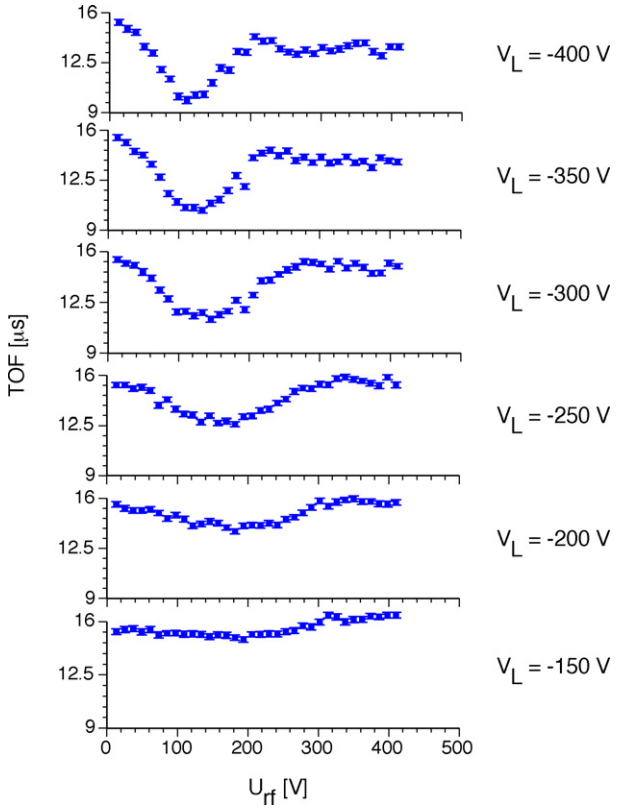


Fig. 24. Time-of-flight as a function of $U_{rf}$ with $\Delta\nu = 0$ using $^{23}Na^+$ with $T_{rf} = 50$ ms octupolar excitation for six different Lorentz steerer voltages, $V_L$. The greater the magnitude of applied voltage, the larger the initial average displacement of the ions from the center of the trap.

function of $U_{rf}$ in the case of $\nu_{rf} = 2\nu_c$ for six different voltages, $V_L$, applied to the Lorentz steerer. The first minimum in the curves represent the necessary $U_{rf}$ to, on average, bring the ions to a state of maximum radial energy.

Fig. 25 plots the beat frequencies observed in Fig. 24 as a function of $\rho_{-,o}$. Two of the curves are simulation results and one is experimental data. The experimental observation does not seem to confirm the nonlinear response illustrated in Fig. 10. However, the $\sigma_{\rho_{-,o}} = 0.13$ mm curve represents our best-fit simulation scenario, and matches the data quite well. The third curve reduces the best-fit value of $\sigma_{\rho_{-,o}}$ by a factor of four to 0.0325 mm. Now the curve begins to recover the nonlinear shape shown in the single ion simulations. Again, the variation of individual beating frequencies of ions in the cloud play a dominant role in determining the overall response of the system.

### 4.3.2. Experimental octupolar resonances

Fig. 26 displays several octupolar resonances of $^{23}Na^+$ produced with $T_{rf} = 50$ ms for various values of $U_{rf}$. Included in the figures are simulated resonances which were produced using the same initial conditions as the simulation in the right column of Fig. 19. For $U_{rf} \leq 40$ V the width of the resonances are between $1.3/T_{rf}$ and $0.9/T_{rf}$. Proceeding towards larger amplitudes reduces this width. At $U_{rf} = 72.9$ V a narrow resonant peak with a width of $\sim 0.2/T_{rf}$ forms atop a broader resonant structure. The narrow peak corresponds to a factor

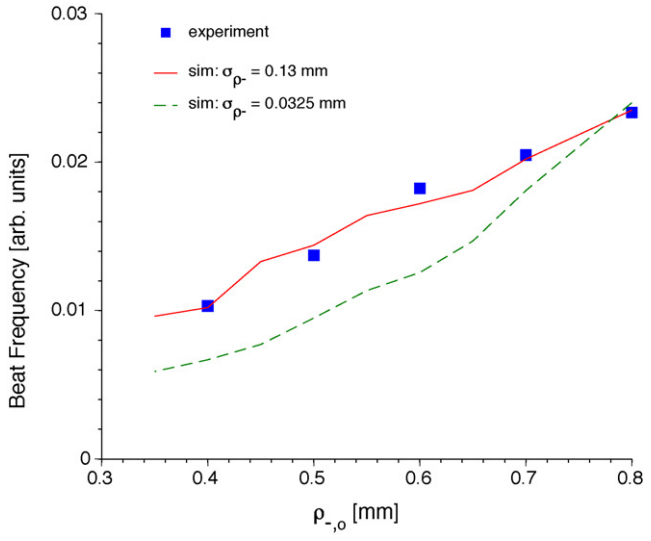


Fig. 25. Beat frequency as a function of $\bar{\rho}_{-,o}$. The experimental curve is extracted from data shown in Fig. 24. The $\sigma_{\rho_{-,o}} = 0.13$ mm curve is a simulation based on the parameters extracted from the simulation shown in Fig. 21. The second simulated curve was generated using identical parameters, except $\sigma_{\rho_{-,o}} = 0.0325$ mm.

of 9 increase in resolving power compared to a comparable quadrupolar excitation.

### 4.3.3. Mass measurements with octupolar excitation

To verify that octupolar resonances can be used for precision mass measurements, a mass measurement of $^{41}K^+$, using $^{39}K^+$

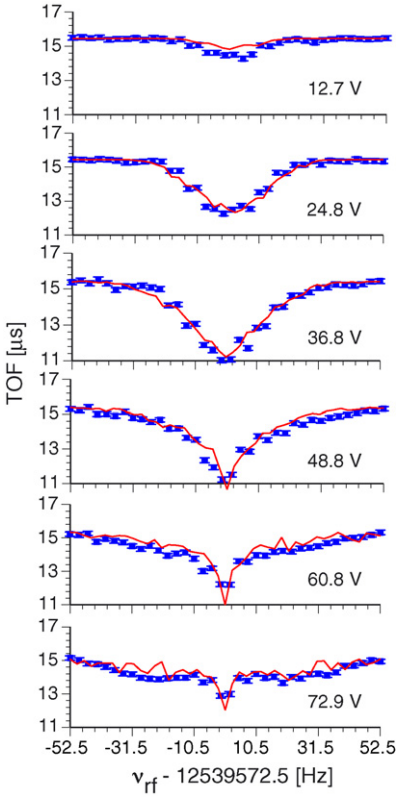


Fig. 26. Several octupolar resonance profiles of $^{23}Na^+$ with $T_{rf} = 50$ ms for various values of $U_{rf}$ (data points) compared with simulated results (solid lines).

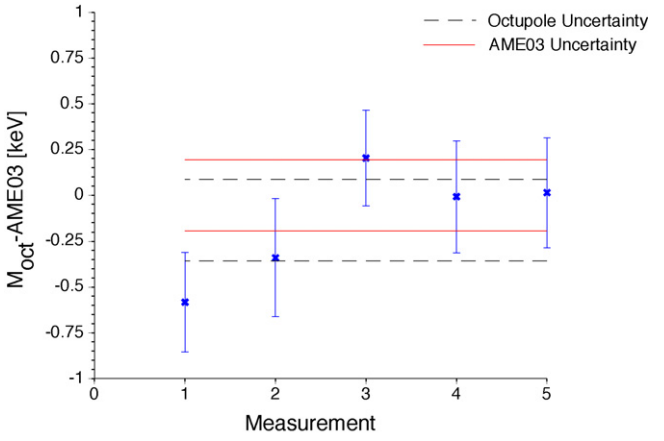


Fig. 27. Mass comparison of $^{39,41}K^+$ using octupolar excitation. $^{39}K^+$ was used as the reference and all measurements were performed with 200 ms excitation times.

as a reference, was performed. An excitation time of $T_{rf} = 200$ ms was used in each individual measurement. $U_{rf}$ was chosen such that the resonances were Gaussian, resembling the resonance shown in Fig. 4. Fig. 27 shows the results of this mass measurement. As there is no theoretical line shape all resonances were fit with a Gaussian profile. What is plotted is the difference of the mean mass value extracted from the octupolar measurements from the accepted literature values (Atomic Mass Evaluation [24]). The dashed lines represent the uncertainty in the mean of the experimental results. The solid lines represent the uncertainty in the AME values. As can be seen, there is excellent agreement within the uncertainty.

## 5. Summary and conclusions

Although an analytical solution to the octupolar excitation has yet to be found, numerical simulations combined with experimental results have offered significant insight into this complicated problem. The most important observations can be summarized as:

- The beat frequency of an ion subjected to an octupolar rf excitation applied at $\nu_{rf} = 2\nu_+ + 2\nu_- = 2\nu_c$ is dependent upon the initial conditions of the ion motion. This is in contrast to the quadrupolar excitation at $\nu_c$ where such a dependence does not exist as long as $\rho_{+,o} = 0$.
- The octupolar resonance profiles have a radically different shape than their quadrupolar counterparts.
- For certain initial conditions it is possible to reduce the width of octupolar resonances by a factor of 10 or more beyond what is achievable with a comparable quadrupolar resonance performed with the same excitation time.

We have experimentally verified a factor of 9 gain in resolving power over the standard quadrupolar excitation scheme. According to simulation, a higher resolving power and a reduced background can be expected if the width of the $\rho_{-,o}$ distribution is reduced. We have also shown that the initial conditions of the ion cloud determines the ultimate resolving power that can be achieved. Although more work is required to assess the absolute accuracy of mass measurements performed with octupolar excitations, a promising first step has been taken towards the implementation of octupolar resonances in high-precision mass measurements. Motivated by the phase dependence exhibited by the octupolar excitation, we have also revisited the quadrupolar excitation and confirmed a phase dependence of resonance line shapes.

## References

[1] M. Bradley, J. Porto, S. Rainville, J. Thompson, D. Pritchard, Phys. Rev. Lett. 83 (1999) 4519.
[2] W. Shi, M. Redshaw, E. Meyers, Phys. Rev. A 72 (2005) 022510.
[3] I. Bergström, C. Carlberg, T. Fritioff, G. Douysset, J. Schonfelder, R. Schuch, Nucl. Instrum. Methods A 487 (2002) 618.
[4] R.S. Van Dyck, Jr., S.L. Zafonte, P.B. Schwinberg, Hyperfine Int. 132 (2001) 163.
[5] G. Bollen, D. Davies, M. Facina, J. Huikari, E. Kwan, P.A. Lofy, D.J. Morrissey, A. Prinke, R. Ringle, J. Savory, P. Schury, S. Schwarz, C. Sumithrarachchi, T. Sun, L. Weissman, Phys. Rev. Lett. 96 (2006) 152501.
[6] A. Kellerbauer, G. Audi, D. Beck, K. Blaum, G. Bollen, B.A. Brown, P. Delahaye, C. Guénaut, F. Herfurth, H.-J. Kluge, D. Lunney, S. Schwarz, L. Schweikhard, C. Yazidjian, Phys. Rev. Lett. 93 (2004) 072502.
[7] G. Bollen, R. Moore, G. Savard, H. Stolzenberg, J. Appl. Phys. 68 (1990) 4355.
[8] M. Kretzschmar, Z. Naturforsch. Teil A 45 (1990) 965.
[9] L. Brown, G. Gabrielse, Rev. Mod. Phys. 58 (1986) 233.
[10] G. Bollen, S. Becker, H.-J. Kluge, M. König, R. Moore, T. Otto, H. Raimbault-Hartmann, G. Savard, L. Schweikhard, H. Stolzenberg, Nucl. Instrum. Methods A 368 (1996) 675.
[11] R. Ringle, P. Schury, T. Sun, G. Bollen, D. Davies, J. Huikari, E. Kwan, D. Morrissey, A. Prinke, J. Savory, S. Schwarz, C. Sumithrarachchi, Int. J. Mass Spectrom. Ion Processes 251 (2-3) (2006) 300.
[12] P. Schury, G. Bollen, D. Davies, A. Doemer, D. Lawton, D. Morrissey, J. Ottarson, A. Prinke, R. Ringle, T. Sun, S. Schwarz, L. Weissman, Eur. Phys. J. A 25 (S1) (2005) 51.
[13] G. Sikler, D. Ackermann, G. Bollen, F. Attallah, D. Beck, J. Dilling, S.A. Eliseev, H. Geissel, D. Habs, S. Heinz, F. Herfurth, Nucl. Instrum. Methods B 204 (2002) 482.
[14] G. Savard, R.C. Barber, D. Beeching, F. Buchinger, J.E. Crawford, S. Gulick, X. Feng, E. Hagberg, J. Hardy, V.T. Koslowsky, J.K.P. Lee, R. Moore, K.S. Sharma, M. Watson, Nucl. Phys. A 368 (1997) 353.
[15] V.S. Kolhinen, T. Eronen, J. Hakala, A. Jokinen, S. Kopecky, S. Rinta-Antila, J. Szerypo, J. Äystö, Nucl. Instrum. Methods Phys. Res. B 204 (2003) 502.
[16] M. König, G. Bollen, H.-J. Kluge, T. Otto, J. Szerypo, Int. J. Mass Spectrom. Ion Processes 142 (1995) 95.
[17] G. Gräff, H. Kalinowsky, J. Traut, Z. Phys. A297 (1980) 35.
[18] J. Dilling, R. Baartman, P. Bricault, M. Brodeur, L. Blomeley, F. Buchinger, J. Crawford, J. Crespo López-Urrutia, P. Delheij, M. Froese, G. Gwinner, Z. Ke, J.K.P. Lee, R. Moore, V. Ryjkov, G. Sikler, M. Smith, J. Ullrich, J. Vaz, T. Collaboration, Int. J. Mass Spectrom. 251 (2006) 198.
[19] S. Schwarz, G. Bollen, D. Lawton, P. Lofy, D.J. Morrissey, J. Ottarson, R. Ringle, P. Schury, T. Sun, V. Varentsov, L. Weissman, Nucl. Instrum. Methods B 204 (2003) 507.
[20] S. Eliseev, M. Block, A. Chaudhuri, F. Herfurth, H.-J. Kluge, A. Martin, C. Rauth, G. Vorobjev, this volume.
[21] G. Bollen, S. Schwarz, D. Davies, P. Lofy, D. Morrissey, R. Ringle, P. Schury, T. Sun, L. Weissman, Nucl. Instrum. Methods A 532 (2004) 203.
[22] T. Sun, S. Schwarz, G. Bollen, D. Lawton, R. Ringle, P. Schury, Eur. Phys. J. A 25 (S1) (2005) 61.
[23] G. Bollen, H.-J. Kluge, T. Otto, G. Savard, L. Schweikhard, H. Stolzenberg, G. Audi, R. Moore, G. Rouleau, J. Mod. Optics 39 (1992) 257.
[24] G. Audi, A.H. Wapstra, C. Thibault, Nucl. Phys. A 729 (2003) 129.